



<http://www.diva-portal.org>

## Postprint

This is the accepted version of a paper published in *European Journal of Pharmaceutical Sciences*. This paper has been peer-reviewed but does not include the final publisher proof-corrections or journal pagination.

Citation for the original published paper (version of record):

Persson, A., Alderborn, G., Frenning, G. (2011)

Flowability of surface modified pharmaceutical granules: A comparative experimental and numerical study.

*European Journal of Pharmaceutical Sciences*, 42(3): 199-209

<http://dx.doi.org/10.1016/j.ejps.2010.11.011>

Access to the published version may require subscription.

N.B. When citing this work, cite the original published paper.

Permanent link to this version:

<http://urn.kb.se/resolve?urn=urn:nbn:se:uu:diva-149033>

# **Flowability of surface modified pharmaceutical granules: a comparative experimental and numerical study**

Ann-Sofie Persson, Göran Alderborn and Göran Frenning\*

*Uppsala University, Department of Pharmacy, Uppsala Biomedical Centre, P.O. Box 580, SE-751 23 Uppsala, Sweden*

\*Corresponding author:

E-mail: Goran.Frenning@farmaci.uu.se, Fax +46 18-471 42 23, Phone +46 18-471 43 75

Flowability – as measured by hopper discharge rate, angle of repose and Carr’s index (CI) – of surface modified microcrystalline cellulose granules was investigated experimentally. Three-dimensional simulations of the granule flow were performed, using the discrete element method (DEM), including either sliding and rolling friction or sliding friction and cohesion in the model. Granule surface modification with polymer coating and lubrication was found to have a significant effect on the sliding friction coefficient. This effect was also reflected in the ensuing flow behaviour, as quantified by the experimental discharge rate and angle of repose, whereas the results for the CI were inconclusive. The numerical results demonstrated that granular flow was qualitatively different for non-cohesive and cohesive granules, occurring in the form of individual particles for the former and in larger blocks for the latter. Rolling friction and cohesion nevertheless affected the simulated discharge rate in a similar manner, producing results comparable to those observed experimentally and calculated with the Beverloo equation. The numerical results for the cohesive granules demonstrated that cohesion alone was sufficient to produce stable heaps. However, the agreement with experimental data was satisfactory only for the non-cohesive granules, demonstrating the importance of rolling friction.

*Keywords:* Discharge rate, Angle of repose, Discrete Element Method, Rolling and sliding friction, Cohesion.

# 1 Introduction

Interparticle forces have a decisive influence on powder flowability (Tykhoniuk et al., 2007). Small forces (relative to gravity) offer less resistance to flow and are most often dominating in systems comprising coarse spherical particles. In pharmaceuticals, free flowing powders are rare and granulation is often required to impart the desired properties. Characterization of flowability can easily be performed by determining the hopper discharge rate (Nedderman et al., 1982) and angle of repose (Train, 1958). Such methods are simple but commonly used in industry and have compendial status (European Pharmacopoeia 7<sup>th</sup> Ed., 2010).

Numerical simulation has lately gained much attention for describing various powder processes. The discrete element method (DEM), originally developed by Cundall and Strack (1979), enables simulations at the particulate level, where particle positions and velocities are traced. The DEM has been used to study both hopper discharge and angle of repose.

From a practical point of view, hopper discharge is typically well-described by the Beverloo equation, which relates the discharge rate to the effective orifice diameter (excluding dead space) to the power of 5/2 (Beverloo et al., 1961). From a more theoretical point of view, a number of studies have demonstrated the ability of the DEM to predict hopper discharge rate, both for spherical (Anand et al., 2008; Datta et al., 2008; Anand et al., 2009) and non-spherical particles (Cleary and Sawley, 2002; Tao et al., 2010). Often 2D (Datta et al., 2008) or quasi-3D (Anand et al., 2008; Anand et al., 2009) systems have been investigated (the latter employing periodic boundary conditions in one spatial direction), but examples of fully-3D simulations exist, especially for non-spherical particles (Cleary and Sawley, 2002; Tao et al., 2010). The studies demonstrated the dependence of discharge rate on hopper angle (Datta et al., 2008) and particle–particle interactions (Anand et al., 2008), including cohesion (Anand et al., 2009). When the DEM is used, friction is typically accounted for by using effective sliding (and rolling) friction coefficients, a practice that we

will adhere to. It is to be noted, however, that stick–slip phenomena may occur when surfaces slide against each other, necessitating a distinction between static and kinetic friction (Bowden and Tabor, 2001).

Although large-scale simulations encompassing up to four million particles have recently been described (Bierwisch et al., 2009), numerical studies of the angle of repose have typically focused on small systems, comprising a few thousand particles, to save computational time (Zhou et al., 1999; Zhou et al., 2001; Zhou et al., 2002; Li et al., 2005). Independent of the size of the simulated system, the importance of frictional forces for accurate prediction of the angle of repose has been demonstrated. Both the sliding (Zhou et al., 2002; Li et al., 2005) and rolling friction coefficients (Zhou et al., 1999; Zhou et al., 2001; Zhou et al., 2002; Bierwisch et al., 2009) significantly affect heap formation and stability. Large friction coefficients decrease the kinetic energy of the particles, thereby prohibiting their translational and rotational motion. Rolling friction is mostly related to particle shape, but a dependence on surface quality and texture exists, as for the sliding friction coefficient. Inclusion of both sliding and rolling friction in the DEM model is essential for accurate prediction of the angle of repose (Zhou et al., 2001; Zhou et al., 2002), at least for non-cohesive particles. Whereas 2D or quasi-3D simulations provide adequate predictions of hopper discharge rate, the angle of repose typically exhibits a pronounced dependence on container thickness (Zhou et al., 2001; Zhou et al., 2002), indicating that fully-3D simulations may be required for realistic results.

Successful comparative studies between experiments and simulations of powder flowability were previously conducted for various materials (Zhou et al., 2002; Li et al., 2005; Datta et al., 2008; Bierwisch et al., 2009). The studies most frequently focused on coarse glass beads and metal powders, whereas pharmaceutical materials received little attention.

However, related processes have been investigated by researchers in the pharmaceutical field, in particular particle packing and die filling (Siiriä and Yliruusi, 2007; Wu, 2008).

The main objective of this work was to appraise the capability of DEM to predict flowability for a pharmaceutically relevant yet relatively simple model material, granulated microcrystalline cellulose (MCC). The granule surfaces – and hence the interparticle forces – were modified by tacky polymer films (Chalykh et al., 2002) and by lubrication. A standard flow testing instrument was used to determine the discharge rate and angle of repose in a combined experiment. These two measures of flowability were extracted from analogous simulations, with the geometry and number of particles chosen to match the experimental work, resulting in fully-3D simulations of an intermediate sized system. A parametric study was performed to further assess the influence of sliding/rolling friction and cohesion on the discharge rate and angle of repose and to see whether cohesion alone may have a similar stabilizing effect on heaps as rolling friction.

## 2 Discrete element model

For simplicity, a linear cohesive model of the type described by Asmar et al. (2002) was used in the simulations. Rolling torques were included, as suggested by Zhou et al. (1999).

### 2.1 Kinematics

Assuming spherical particles, each particle  $i$  is characterized by its radius ( $R_i$ ), mass ( $M_i$ ), centre-of-mass position ( $\mathbf{x}_i$ ), linear velocity ( $\mathbf{v}_i$ ), and angular velocity ( $\boldsymbol{\omega}_i$ ). Focusing on contact between two particles 1 and 2 (Fig. 1), the relative position vector  $\mathbf{x}_{12} = \mathbf{x}_1 - \mathbf{x}_2$  is used to determine particle normals ( $\hat{\mathbf{n}}_i$ ) as

$$\hat{\mathbf{n}}_1 = -\hat{\mathbf{n}}_2 = -\frac{\mathbf{x}_{12}}{|\mathbf{x}_{12}|}. \quad (1)$$

The radii vectors  $\mathbf{r}_i = R_i \hat{\mathbf{n}}_i$  ( $i = 1, 2$ ) enable the surface velocity of the particles at the contact point ( $\mathbf{v}_i^s$ ) to be determined as

$$\mathbf{v}_i^s = \mathbf{v}_i + \boldsymbol{\omega}_i \times \mathbf{r}_i \quad (i = 1, 2). \quad (2)$$

Relative velocities are introduced as  $\mathbf{v}_{12} = \mathbf{v}_1 - \mathbf{v}_2$  and  $\mathbf{v}_{12}^s = \mathbf{v}_1^s - \mathbf{v}_2^s$ , and the relative surface velocity is decomposed into normal and tangential components,  $\mathbf{v}_{12}^{sn} = (\mathbf{v}_{12}^s \cdot \hat{\mathbf{n}}_1) \hat{\mathbf{n}}_1$  and  $\mathbf{v}_{12}^{st} = \mathbf{v}_{12}^s - \mathbf{v}_{12}^{sn}$ , respectively. Elastic contact forces are determined from the normal and tangential overlaps, which are defined as  $\delta_n = R_1 + R_2 - |\mathbf{x}_{12}|$  and  $\delta_t = |\mathbf{u}_{12}|$ . Here,  $\mathbf{u}_{12}$  is the tangential displacement of particle 1 relative to particle 2, initialized as zero when the particles first touch and during the lifetime of the contact updated via

$$\dot{\mathbf{u}}_{12} = s \mathbf{v}_{12}^{st} + \frac{(\mathbf{u}_{12} \cdot \mathbf{v}_{12})}{|\mathbf{x}_{12}|} \hat{\mathbf{n}}_1, \quad (3)$$

where  $s = 1$  for stick and  $s = 0$  for slip (see below) and the superposed dot denotes the time derivative. The second term in Eq. (3) takes into account changes in  $\mathbf{u}_{12}$  that occur when both particle rotate around a common axis (Luding, 2008). Based on the tangential relative displacement, tangential unit vectors ( $\hat{\mathbf{t}}_i$ ) are introduced as

$$\hat{\mathbf{t}}_1 = -\hat{\mathbf{t}}_2 = \frac{\mathbf{u}_{12}}{|\mathbf{u}_{12}|}. \quad (4)$$

Note that the sign conventions used in Eqs. (1) and (4) are such that repulsive normal and frictional tangential forces on particle 1 are directed along the *negative*  $\hat{\mathbf{n}}_1$  and  $\hat{\mathbf{t}}_1$  directions.

## 2.2 Forces

The force  $\mathbf{F}_{12}$  on particle 1 caused by particle 2 may generally be expressed as

$$\mathbf{F}_{12} = -(f_n \hat{\mathbf{n}}_1 + f_t \hat{\mathbf{t}}_1 + c_n \mathbf{v}_{12}^{sn} + c_t \mathbf{v}_{12}^{st}), \quad (5)$$

where  $f_n$  and  $f_t$  are scalar elastic normal and tangential forces and  $c_n$  and  $c_t$  are normal and tangential damping coefficients.

### 2.2.1 Normal elastic forces

Overlapping particles ( $\delta_n > 0$ ) are assumed to experience a repulsive normal force of magnitude

$$f_n = K_n \delta_n, \quad (6)$$

where  $K_n$  is a normal stiffness. In addition, cohesive particles in close proximity are assumed to attract each other. In this case, Eq. (6) is applied for all  $\delta_n > \delta_n^{\min} = -K_c \Delta R / (K_n + K_c)$ , where  $K_c$  is a cohesive stiffness and  $\Delta R$  is a cut-off distance (Fig. 2). In addition,

$$f_n = -K_c (\delta_n + \Delta R) \quad (7)$$

when  $-\Delta R < \delta_n < \delta_n^{\min}$ . It may be noted that the maximal attractive force has magnitude  $f_c = -f_n^{\min} = K_n K_c \Delta R / (K_n + K_c)$ , and this value may be used to calculate the granular Bond number (Nase et al., 2001) as  $\text{Bo}_g = f_c / f_g$ , where  $f_g$  is the magnitude of the force due to gravity.

### 2.2.2 Tangential elastic forces

Tangential forces are experienced by overlapping particles only. In accordance with Coulomb friction, we set

$$f_t = \min(K_t \delta_t, \mu_s f_n) \quad (8)$$

where  $K_t$  is a tangential stiffness and  $\mu_s$  is a sliding friction coefficient. Thus particles stick to each other when  $K_t \delta_t < \mu_s f_n$  and slip when  $K_t \delta_t > \mu_s f_n$ .

### 2.2.3 Contact damping

Normal contact damping is applied whenever two particles interact, with a damping coefficient  $c_n = 2\gamma_n\sqrt{M_{\text{eff}}K_n}$ , where  $\gamma_n$  is a predetermined fractional damping coefficient and  $M_{\text{eff}} = M_1M_2/(M_1 + M_2)$  is the effective mass. Tangential damping is applied only when stick occurs, in which case  $c_t = 2\gamma_t\sqrt{M_{\text{eff}}K_t}$ , with  $\gamma_t$  being the fractional tangential damping coefficient.

## 2.3 Torques

The torque  $\mathbf{T}_{12}$  on particle 1 caused by contact with particle 2 is determined as

$$\mathbf{T}_{12} = \mathbf{r}_1 \times \mathbf{F}_{12} - \mu_r f_n \hat{\boldsymbol{\omega}}_1 \quad (9)$$

where the first term corresponds to the standard torque caused by the contact force  $\mathbf{F}_{12}$ . The second term represents a rolling torque (Zhou et al., 1999), with  $\mu_r$  being a rolling friction coefficient and  $\hat{\boldsymbol{\omega}}_1 = \boldsymbol{\omega}_1/|\boldsymbol{\omega}_1|$  an appropriate unit vector.

## 2.4 Equations of motion

For spherical particles, balance of linear and angular momentum may be expressed as

$$M_i \dot{\mathbf{v}}_i = \mathbf{F}_i, \quad (10)$$

$$I_i \dot{\boldsymbol{\omega}}_i = \mathbf{T}_i, \quad (11)$$

where  $I_i = (2/5)M_iR_i^2$  is the moment of inertia. The total force  $\mathbf{F}_i$  on particle  $i$  has contributions from gravity and contact with other particles and confining surfaces (when appropriate). The total torque  $\mathbf{T}_i$  is similarly assembled from contact contributions. The

equations of motion are integrated explicitly as per the standard DEM (Cundall and Strack, 1979).

### 3 Materials and methods

#### 3.1 Materials

MCC granules, Cellets<sup>®</sup> 350 (hereafter referred to as uncoated granules), with a size distribution of 350–500  $\mu\text{m}$  were purchased from HARKE Pharma GmbH, Germany. Polyethylene glycol 6000 (Sigma-Aldrich, Germany) and Kollidon<sup>®</sup> 17 PF (BASF, Germany), hereafter referred to as PEG and PVP. The apparent particle density ( $n=2$ ) of MCC (1.57  $\text{g}/\text{cm}^3$ ), PEG (1.23  $\text{g}/\text{cm}^3$ ) and PVP (1.19  $\text{g}/\text{cm}^3$ ) were measured with helium pycnometry (AccuPyc 1330, Micrometrics, USA). Magnesium stearate was used as lubricant.

#### 3.2 Granule surface modification

The interparticle forces were modulated by modifying the granule surfaces with PEG, PVP and magnesium stearate.

Granules, in an amount of 200 g, were coated with 24 g of various proportions of PEG and PVP (Table 1) using a fluid bed coater (STREA-1, Aeromatic, MuttENZ, Switzerland) equipped with a 20 cm Wurster column and a 0.5 mm spray nozzle. The polymer amounts used would produce a nominal film thickness,  $h$ , of 10  $\mu\text{m}$ , as obtained from the equation

$$w_{\text{mix}} = \rho_{\text{mix}} \cdot S_V \cdot V \cdot h, \quad (12)$$

where  $w_{\text{mix}}$  and  $\rho_{\text{mix}}$  are the weight and apparent density of the polymers in the coating liquid,  $S_V$  is the nominal volume specific surface area of the granules (determined from their average size 425  $\mu\text{m}$ ) and  $V$  is the total effective volume of the granules (Tunón et al., 2003). For solutions containing both PEG and PVP the apparent particle density was calculated as described earlier (Jerwanska et al., 1995). The atomizing pressure was set to 1.0 bar to

produce a mist, which was evenly distributed over the granules. The spray rate  $\sim 1$  ml/min was chosen to reduce the likelihood that granules formed secondary agglomerates. After coating, the granules were first dried in the air flow for 3 minutes and secondly at room temperature for a minimum of 5 days before sieving to remove agglomerates larger than 710  $\mu\text{m}$ .

In order to decrease the interparticle forces, 200 g granules were mixed with 0.2 g magnesium stearate in a Turbula mixer (Willy A. Bachofen, Basel, Switzerland) for 100 minutes at 96 rpm.

The granules were stored in a desiccator at 40 % RH (over a saturated  $\text{K}_2\text{CO}_3$  solution) at room temperature ( $\sim 20$  °C) for at least 5 days before any measurements were performed.

### **3.3 Granule characterization**

#### **3.3.1 Granule size**

Granules were carefully spread out and separated on a flatbed scanner (Epson Perfection 1640SU Scanner, Seiko Epson Corp., Japan) and covered by a black background ( $n > 1000$ ). Images (1600 dpi) were captured and analyzed using ImageJ (Abramoff et al., 2004). The granules were assumed spherical and the granule diameter was calculated from the measured projected area.

#### **3.3.2 Particle density**

The apparent particle density was calculated in the same manner as the polymer densities. The effective particle density (including both open and closed pores) was measured with mercury pycnometry (Autopore III 9420, Micrometrics, USA) as described earlier ( $n=2$ ) (Wikberg and Alderborn, 1990). To facilitate the degassing step the granules were stored in a desiccator at low relative humidity (over silica gel) at room temperature for at least 5 days prior to the

analysis. The porosity was calculated as one minus the ratio between the effective and apparent particle densities.

### **3.3.3 Bulk density**

Granules (39–45 g) were manually poured through a funnel into a measuring cylinder (21.7 mm diameter) and weighed (Delta Range B3002, Mettler Toledo, Switzerland) to obtain the bulk density,  $\rho_{\text{bulk}}$  ( $n=3$ ). The granule bed was subjected to 500 taps (PharmaTest, PT-TD, Hainburg, Germany) to determine the tap density,  $\rho_{\text{tap}}$ . 500 taps were considered adequate because all significant changes in powder volume occurred during the first 100 taps.

### **3.3.4 External surface area**

Steady-state air permeametry ( $n=3$ ) was used to determine the volume specific external surface area for all granule types. The granules were poured into a cylinder with a height and diameter of 150 mm and 11.47 mm, respectively, and both the weight and height were recorded. The cylinder was connected to a pump, which controlled the air flow rates through the granule bed (Brook flow meter, Brook Instruments B. V., the Netherlands). The pressure in the granule bed was measured from high to low air flow with a manometer (P 200 S, Digitron Instrumentation Ltd, UK). The area was calculated as described earlier using the Kozeny-Carman equation and an aspect factor of 6 (Eriksson et al., 1993).

### **3.3.5 SEM images**

Scanning electron microscopy, SEM, images of the granules were acquired to enable visualization of the shape and surface of the coated particles. The granules were first attached onto metal stubs by double-adhesive tape and then sputtered with gold (JEOL JFC-1100, Tokyo, Japan). The images were captured at three magnifications, low (71–73  $\times$ ), medium

(280–370 ×) and high (10 000 ×), using the SEM microscope (LEO 1530 Gemini, Leo, UK) at an accelerating voltage of 3.0 kV.

### 3.3.6 Sliding friction coefficients

Sliding friction coefficients between different types of granules and both smooth MCC tablets and regular paper were determined with a sloping plane, as a simple means of assessing friction against cellulose surfaces of different roughness. Tablets (20mm Ø) were compressed with a materials tester with a maximal applied force of 50 kN (Zwick Z100, Zwick/Roell GmbH & Co. KG, Ulm, Germany). A granular monolayer ( $n=10$ ) was attached to adhesive tape and placed under normal load onto a tablet ( $n=10$ ) or a piece of paper ( $n=60$ ) fixed to the plane. The plane was connected by a string to a texture analyzer (TA HDi Texture Analyser, Stable Micro Systems, UK) at one end and hinged to a table at the other end. The height at which the plane obtained a slope where the granules began to slide was measured. The height was used for calculations of the plane angle,  $\theta$ , which was the basis for determination of the sliding friction coefficient,  $\mu_s = \tan \theta$ .

## 3.4 Flowability measurements

### 3.4.1 Carr's index

The bulk and the tapped densities were used for calculation of Carr's compressibility index, CI (Carr, 1965):

$$CI = \frac{\rho_{tap} - \rho_{bulk}}{\rho_{tap}} \times 100. \quad (13)$$

### 3.4.2 Hopper discharge rate and angle of repose

The experimental determination of flowability was performed by using a Pharma Test PTG-2 (Hainburg, Germany) flow testing instrument that measured flow times and angles of repose in a single experiment. As illustrated in Fig. 3, the instrument basically consisted of a cylindrical–conical hopper, a conical nozzle, and a circular collector plate made of polyoxymethylene plastic. In addition, a cylindrical cavity was present in between the nozzle and the “release flap,” which closed the lower orifice during filling and was removed when the experiment started. 13 ml of granules were used in each experiment ( $n=3$ ). The discharge rate was determined as the ratio between the bulk mass of discharged granules and the flow times.

### **3.5 Flow simulations**

The same geometrical setup as in the experiments (Fig. 3) was used for the simulations. Flow of non-cohesive granules was simulated for a range of sliding and rolling friction coefficients. Particle–wall interactions are known to have a relatively minor impact on the flow, due to limited contact between the particles and the wall (Anand et al., 2008), and the frictional force has been claimed to depend primarily on the particle properties rather than on the substrate surface properties (Podczec et al., 1995). For these reasons, the friction coefficients were assumed to be the same for the particle–particle and particle–wall interactions. Flow of cohesive granules was simulated for a range of sliding friction coefficients, without any rolling friction, with cohesion being characterized by the granular Bond number. The latter simulations were performed for two different values of the cut-off distance  $\Delta R$  (0.1 and 1  $\mu\text{m}$ ). To reduce the simulation times, particles that could no longer affect the discharge rate or the formation of a heap on the collector plate were removed.

Parameters that were kept fixed in all simulations are collected in Table 2. The particle density was determined from the apparent density of MCC, using a granule porosity of 10 %,

and the particle diameter was based on the manufacturer's specifications. Whereas particle number ( $N$ ), diameter ( $d_p$ ) and density ( $\rho$ ) may be considered as known, the normal and tangential stiffness ( $K_n$  and  $K_t$ ) were estimated based on a consideration of particle interpenetration and stability of the solution procedure (the selected time-step  $\Delta t$  is about 3 times smaller than  $\sqrt{M/K}$ , where  $M$  is the particle mass). One advantage of the linear contact model employed in this work is that the normal and tangential velocity profiles during contact are independent of the stiffness, indicating that the stiffness has a limited influence on the overall particle dynamics (Di Renzo and Di Maio, 2004). The stiffness does however influence the high-frequency behaviour and hence the critical time step. In order to keep the simulation times within reasonable bounds, a stiffness considerably lower than the one calculated from experimental data for MCC was therefore used. Although the particles in this work are assumed to interact by purely elastic forces, the maximal stiffness is in practice limited by the onset of plastic deformation. An estimate based on the elastic-plastic model of Thornton and Ning (1998), using experimental data for similarly prepared granules from literature (Nordstrom et al., 2008), indicates that the stiffness has been scaled down by 2 to 3 orders of magnitude. A similar stiffness scaling has previously been used to simulate mixing of MCC granules (Lemieux et al., 2007). Typical values, previously used for MCC granules (Lemieux et al., 2007), were assumed for the normal and tangential fractional damping coefficients ( $\gamma_n$  and  $\gamma_t$ ).

Initial configurations were generated by letting particles settle under the influence of gravity until a stable pack was obtained, as inferred from their root-mean-square (RMS) velocity (with the limit set to 10  $\mu\text{m/s}$ ). For the assumed particle size and number (Table 2), the initial pack extended about 33 mm above the release flap, i.e., almost up to the boundary between the conical and cylindrical hopper regions. It may be noted that a similar number of particles were used in the simulations as in the experiments. During the course of the

simulations, the number of particles that had passed the orifice was recorded at certain instants of time, and the simulated discharge rate was calculated from the slope of the linear part of the amount discharged–time curves. The simulations were considered done once the RMS velocity of the particles was smaller than 10  $\mu\text{m/s}$  and the angle of repose was then calculated from the ensuing heap.

The simulations were run on a dedicated HP ProLiant DL585 G5 server, equipped with four quad-core AMD Opteron processors (model 8356) operating at 2.3 GHz, and a total of 8 GB of RAM. Our DEM implementation relies on the standard Message Passing Interface (MPI) and uses an adaptive domain-decomposition algorithm based on orthogonal recursive bisection (Salmon, 1990) to achieve a good parallel performance. Each simulation nevertheless typically required 1 to 2 days to complete.

### 3.6 Calculation of Beverloo discharge rates

For a flat-bottomed hopper, the Beverloo discharge rate can be calculated from the particle diameter ( $d_p$ ), orifice diameter ( $D_0$ ), and bulk density ( $\rho_{\text{bulk}}$ ) by using Eq. (14) (Beverloo et al., 1961),

$$W = C\rho_{\text{bulk}}\sqrt{g}(D_0 - kd_p)^{5/2}, \quad (14)$$

where  $g$  is the acceleration due to gravity. The equation contains two parameters, the discharge coefficient  $C$  which usually is about 0.58 and  $k$  that represents the shape coefficient with a value of 1.5 for spherical granules (Nedderman, 1992). The hopper shape is known to affect the Beverloo discharge rate, and a geometrical correction factor is needed for a cylindrical hopper. This factor was in this work calculated as suggested by Brown and Richards (1965) as 1.15. Various opinions exist regarding the most appropriate bulk density to be used in the Beverloo equation. According to the original work, the bulk density should be determined after particle packing (Beverloo et al., 1961). Verghese and Neddermann (1995)

on the other hand stated that the flow density should be used since the particle bed dilates during discharge (Nedderman et al., 1982). In this work, the poured bulk density was used in the calculations, which has been proven to be a realistic estimate of the flow density (Datta et al., 2008).

## **4 Results and discussion**

### **4.1 Experimental results**

#### **4.1.1 Granule characteristics**

The granular size distributions are shown in Fig. 4. The granules may be divided into two groups; the uncoated and lubricated ones with a particle size of about 440  $\mu\text{m}$  and the polymer coated ones with a size of about 460  $\mu\text{m}$ . Since the granule diameter is determined from a projection of the granules in their most stable position, the obtained values are expected to be somewhat larger than those obtained by other methods. However, the size distribution is favourably compared with the size range specified by the manufacturer.

By utilizing the difference in median particle size, the thickness of the coating layers was calculated (Table 3). The polymer coatings display film thicknesses of about 10  $\mu\text{m}$ , in good agreement with the estimate based on nominal granule surface area. The increased particle size is also reflected in the decreased volume specific surface areas for the coated granules compared to the uncoated and lubricated ones.

The intragranular porosity was determined for the uncoated granules, for which the apparent particle density was known. Granules prepared from MCC using water as granulation liquid are expected to have a low porosity (Johansson et al., 1995), which was indeed obtained for the uncoated granules (Table 3).

The granule shape and surface texture may be inferred from the SEM images provided in Fig. 5. The granule surfaces generally appeared smoother after coating, as seen at high

magnification in the insets. Polymer coatings containing 0–10 % PVP (Fig. 5b–d) resulted in granules of more irregular shape compared to the other granule types, which retained the smooth spherical shape. For the irregular granules, low magnification images revealed occasional granule aggregation into pairs (images not shown).

Sliding friction coefficients obtained from granules in contact with a smooth tablet surface and a rougher paper are given in Table 4. These values are provided as effective measures of sliding friction and as an indication of the expected range for the friction coefficients. For granules in contact with tablet surfaces significantly ( $p < 0.05$ ) higher sliding friction coefficients were obtained for the polymer coated granules in comparison with the uncoated ones. However, no significant differences were observed between the polymer coatings. All values obtained were relatively small, which is interpreted as resulting from the smooth tablet surface.

The friction coefficients for granules in contact with paper were in the same range as those used in the numerical analysis. Based on the estimated granule–paper friction coefficients, the granules could be classified into three groups: (1) granules displaying similar  $\mu_s$  as the uncoated ones (PEG/PVP 95/5 and magnesium stearate), (2) granules displaying higher  $\mu_s$  compared to (1) (PEG 100 and PEG/PVP 50/50), and (3) PEG/PVP 90/10 coated granules which obtained the highest  $\mu_s$ .

#### **4.1.2 Granular flow properties**

All granules were considered as free flowing based on results for experimental hopper discharge rate, angle of repose and CI (Table 5). The flowability was however influenced by the granular surface modification. PEG coating contributed to decreased flowability as inferred from the decreased experimental discharge rate and the increased angle of repose. Incorporation of PVP in the coating layer was expected to decrease the flowability further in a

concentration-dependent manner (Chalykh et al., 2002), but no clear trend was detected in this work. The largest angle of repose was observed for granules containing 10 % PVP in the coating, which is consistent with the granule–paper sliding friction coefficient. It may be noted that the inclusion of 50 % PVP in the coating smoothed the granule surfaces but retained the spherical shape, as indicated by the SEM images (compare Fig. 5e with Fig. 5a), and thereby increased the experimental discharge rate and decreased the angle of repose. Since the granule–paper sliding friction coefficient is not particularly low for this coating, the increased flowability is most likely related to a low rolling friction coefficient.

The decreased flowability obtained for the polymer coatings containing 0–10% PVP may be considered as the result of the irregular shapes observed in Fig. 5b-d, partly due to increased rolling friction (Zhou et al., 2002) and mechanical interlocking. To completely explain the flow behaviour, the sliding friction alone is not sufficient and the inclusion of rolling friction and/or cohesion forces is hence required.

Lubrication provided unchanged sliding friction coefficients compared to uncoated granules. However, the experimental discharge rate was increased and heap formation was prohibited, again demonstrating the importance of including other interparticle forces than those resulting from sliding friction.

Somewhat surprisingly, the CI (Table 5) decreased slightly after coating. Such a decrease is generally taken to be an indicator of an improved flowability (Carr, 1965), and the CI typically increase as the angle of repose increases (Geldart et al., 2006). For the granules investigated in this work, inferences based on the CI contradict the observed flow behaviour as quantified by the discharge rates and angles of repose, suggesting that the CI is not a representative indicator of the granular flow. However, since polymer coating not only affected the surface characteristics of the granules but also increased their size by about 20  $\mu\text{m}$ , an effect of particle size on flow rate cannot be excluded. The increased granule size

is expected to correspond to a reduction of the flow rate by less than 3 %, as inferred from the Beverloo Eq. (14), which is not sufficient to explain the experimental results. Nevertheless, a comparison of the CI within each of the two size groups (the uncoated/lubricated and polymer coated granules) reveals that the CI decreases with increasing discharge rate, as would generally be expected.

The small changes in the CI observed were most likely an effect of the spherical granule shape, which resulted in a close granule packing both before and after surface modification. An additional explanation of these observations is provided in section 4.4.

## **4.2 Numerical parametric study**

### **4.2.1 Noncohesive particles: effect of sliding and rolling friction**

As expected, the inclusion of frictional forces in the 3D numerical model altered the flowability properties of the simulated granules. Both the sliding ( $\mu_s$ ) and rolling friction ( $\mu_r$ ) influenced the simulated discharge rate and angle of repose (Fig. 6).

A fairly linear decrease in simulated discharge rate was observed with increasing rolling friction coefficients (Fig. 6a). In addition, an increased  $\mu_s$  decreased the discharge rate of the simulated granules, in a manner virtually independent of the magnitude of the rolling friction. This finding indicates that the resistances to translational and rotational motion – governed by  $\mu_s$  and  $\mu_r$  – have an additive effect on the simulated discharge rate, at least in the investigated parameter ranges.

Nearly linear increases in angles of repose with increasing  $\mu_r$  were observed for intermediate and high  $\mu_s$  (Fig. 6b). For the smallest  $\mu_s$ , rolling friction exceeding a threshold value of 2.0  $\mu\text{m}$  was required for heap formation. It may also be noted that a considerable increase of rolling friction is necessary for the formation of more stable heaps and hence

higher angles of repose. These results are in agreement with previous studies investigating the effects of sliding and rolling friction on heap formation (Zhou et al., 1999; Zhou et al., 2001).

As will be discussed in more detail below, there is a clear negative correlation between angles of repose and discharge rates, indicating that these two measures provide consistent information on the granule flowability. The simulated granule flow for non-cohesive granules is illustrated in Fig. 7a ( $\mu_s=0.6$  and  $\mu_r=2 \mu\text{m}$ ). A continuous flow of individual granules is seen and the resulting heap is low with a convex appearance as was also observed in the experimental measurements.

#### **4.2.2 Cohesive particles: effect of sliding friction**

The magnitude of the cohesion force was quantified by the granular Bond number,  $Bo_g$ , and its spatial extent by the cut-off distance,  $\Delta R$  (Fig. 2). Although flow simulations were performed for two values of  $\Delta R$  (0.1 and 1  $\mu\text{m}$ ), the following discussion is largely restricted to  $\Delta R = 1 \mu\text{m}$ . The effect of cohesion on the simulated discharge rate was insignificant for the smaller cut-off distance (data not shown) and consistent heap formation was only observed for the highest sliding friction coefficient ( $\mu_s = 0.8$ ) when the smaller cut-off distance was used. Whereas van der Waals forces typically are insignificant at distances exceeding  $\sim 100 \text{ nm}$ , liquid bridges may extend further (see, e.g., the review by Seville et al. (2000) and references therein). The results for the smaller cut-off distance may hence reflect the underlying physics, but a numerical effect cannot be ruled out, since very small time steps would be required to accurately integrate short-range forces.

For the larger cut-off distance, an increased  $Bo_g$  decreased the simulated discharge rate, irrespective of the sliding friction coefficient (Fig. 8a). From the results presented in Fig. 8b, it is evident that cohesion alone was sufficient to produce stable heaps – since rolling friction was not included in the simulations for cohesive particles – but threshold values were observed for both the low and intermediate sliding friction coefficients.

In general terms, rolling friction and cohesion appear to have a similar effect on the discharge rate (compare Figs. 6a and 8a), whereas their effect on angle of repose is somewhat different (compare Figs. 6b and 8b). The mechanisms of action must be different in both cases, however, since cohesion produces an attractive normal force whereas rolling friction is related to the tangential force. Flow of cohesive powders is often claimed to occur in coherent clusters much larger than the particle size (Castellanos, 2005), and such clusters are indeed evident in Fig. 7b, which illustrates the simulated granule flow for cohesive granules ( $\mu_s=0.6$  and  $Bo_g=2$ ). Similar observations have previously been made in quasi-3D simulations of discharge of cohesive particles (Anand et al., 2009).

### **4.3 Comparison with Beverloo discharge rates**

The Beverloo discharge rates (Table 5) accounts for interparticle forces in an indirect manner, via their influence on the bulk density. As indicated by Spearman's rank correlation coefficient – calculated as 0.84 ( $p<0.05$ ) – there is a reasonable, but not perfect, agreement between the Beverloo and experimental discharge rates for the different granule types. The discrepancy is most likely due to the fact that the parameters  $C$  and  $k$  were considered as standard and hence not determined for the various granules. Moreover, different procedures to correct for the hopper geometry exist in the literature (Anand et al., 2009).

The Beverloo discharge rates may also be compared to the numerical results for the non-cohesive granules, but a modification of Eq. (15) would be required for the cohesive ones (Nedderman, 1992; Anand et al., 2009). The range of Beverloo discharge rates is relatively narrow (3.4–3.9 g/s), and values in this range were obtained for all sliding friction coefficients, provided that the rolling friction was appropriately selected, indicating a good general agreement between Beverloo and simulated values. More detailed comparisons were unfortunately not possible, because the rolling friction could not be independently determined.

#### **4.4 Comparison between experiments and simulations**

As demonstrated by the experimental sliding friction coefficients, the surface modifications affected the interparticle forces, and the range obtained for the experimental sliding friction coefficients was similar to the one used in the simulations.

In order to unambiguously compare experiments and simulations, the experimentally and numerically determined angles of repose were displayed a function of the corresponding discharge rates. The simulations performed with rolling friction but not cohesion included in the model produced results in satisfactory agreement with experiments (Fig. 9a), especially for the intermediate and high sliding friction coefficients, indicating that the non-cohesive DEM model captured the essential features of the experimental granular flow. However, the data do not admit firm conclusions regarding the importance of sliding and rolling friction for the behaviour of the experimental system. On the other hand, when cohesion but not rolling friction was included in the model, the angle of repose was consistently overestimated by the numerical results (Fig. 9b). Although cohesion slowed down simulated hopper discharge in a similar manner as rolling friction, and was sufficient to produce stable heaps, it may be concluded that rolling friction is required for a good quantitative agreement with experimental results. An effect of cohesion on the experimental flow is still possible, but rolling friction clearly dominated for the relatively large agglomerates investigated experimentally.

The importance of rolling friction for the experimental system may explain the results for the CI: Rolling friction may have influenced the CI by locking the particle positions in the granule bed, disabling rolling and further packing during tapping. The CI would probably have been more representative measures of granular flow for a system dominated by cohesive forces.

## **5 Conclusion**

Flowability – as measured by hopper discharge rate, angle of repose and CI – of surface modified MCC granules was investigated experimentally. Fully-3D DEM simulations of the granule flow were performed, including either sliding and rolling friction or sliding friction and cohesion in the model. Granule surface modification with polymer coating and lubrication was found to have a significant effect on the sliding friction coefficient. This effect was also reflected in the ensuing flow behaviour, as quantified by the experimental discharge rate and angle of repose. For the experimental system comprising coarse nearly spherical granules, the CI were, on the other hand, found not to be representative measures of the flowability, but the increased granule size imparted by polymer coating may partly explain this observation. The numerical results for the non-cohesive granules indicated that sliding and rolling friction – and hence the resistance to translational and rotational motion – may be considered to have an additive effect on the simulated discharge rate. Rolling friction and cohesion both affected the simulated discharge rate in a similar manner, producing results comparable to those observed experimentally and calculated with the Beverloo equation. The flow was qualitatively different in the two cases, however, occurring in the form of individual particles for non-cohesive granules and in larger blocks for the cohesive ones. The numerical results for the cohesive particles demonstrated that cohesion alone was sufficient to produce stable heaps. Still, the agreement with experimental data was satisfactory only for the non-cohesive granules, demonstrating that rolling friction dominated over cohesion for the experimental system.

## **Acknowledgments**

The authors wish to thank Leif Ljung (Department of Medical Cell Biology, Uppsala University) for preparation of the SEM images. Financial support to this investigation

provided by the Swedish Research Council (Project No. 621-2007-3854) is hereby gratefully acknowledged.

## Notation

An upright bold font is used for vectors. The scalar (dot) product of two vectors  $\mathbf{u}$  and  $\mathbf{v}$  is written as  $\mathbf{u} \cdot \mathbf{v}$  and the vector (cross) product as  $\mathbf{u} \times \mathbf{v}$ . A unit vector in the direction of a nonzero vector  $\mathbf{u}$  is written as  $\hat{\mathbf{u}}$ . Time derivatives are indicated by superposed dots.

$Bo_g$	granular Bond number
$c_n$	normal damping coefficient
$c_t$	tangential damping coefficient
$C$	discharge coefficient in Beverloo Eq.
$CI$	Carr's compressibility index
$d_p$	particle diameter
$D_0$	orifice diameter
$f_c$	magnitude of maximal attractive force
$f_g$	magnitude of force due to gravity
$f_n$	scalar elastic normal force
$f_n^{\min}$	value of $f_n$ at $\delta_n^{\min}$
$f_t$	scalar elastic tangential force
$\mathbf{F}_i$	total force on particle $i$
$\mathbf{F}_{12}$	force on particle 1 caused by particle 2
$g$	acceleration due to gravity
$h$	(nominal) film thickness
$I_i$	moment of inertia of particle $i$
$k$	shape coefficient in Beverloo Eq.
$K_c$	cohesive stiffness
$K_n$	normal stiffness
$K_t$	tangential stiffness

$M_i$	mass of particle $i$
$M_{\text{eff}}$	effective mass
$n$	number of independent repeated measurements
$N$	number of particles
$\hat{\mathbf{n}}_i$	unit normal vector of particle $i$ at contact point
$p$	$p$ -value in significance tests
$\mathbf{r}_i$	radius vector of particle $i$
$R_i$	radius of particle $i$
$\Delta R$	cut-off distance for attractive force
$s$	indicator variable of stick or slip
$S_V$	(nominal) volume-specific surface area
$\Delta t$	time step used in numerical solution
$\hat{\mathbf{t}}_i$	unit tangent vector of particle $i$ at contact point
$\mathbf{T}_i$	total torque on particle $i$
$\mathbf{T}_{12}$	torque on particle 1 caused by particle 2
$\mathbf{u}_{12}$	tangential relative displacement
$\mathbf{v}_i$	velocity of particle $i$
$\mathbf{v}_{12}$	relative velocity
$\mathbf{v}_i^s$	surface velocity of particle $i$ at contact point
$\mathbf{v}_{12}^s$	relative velocity of contact points
$\mathbf{v}_{12}^{\text{sn}}$	normal component of $\mathbf{v}_{12}^s$
$\mathbf{v}_{12}^{\text{st}}$	tangential component of $\mathbf{v}_{12}^s$
$V$	total volume of granules
$w_{\text{mix}}$	weight of polymers in the coating liquid
$W$	Beverloo discharge rate
$\mathbf{x}_i$	centre-of-mass position of particle $i$
$\mathbf{x}_{12}$	relative particle position

## Greek letters

$\gamma_n$	fractional normal damping coefficient
$\gamma_t$	fractional tangential damping coefficient
$\delta_n$	normal overlap
$\delta_n^{\min}$	location of minimum in force–overlap curve
$\delta_t$	tangential overlap
$\theta$	plane angle
$\mu_r$	rolling friction coefficient
$\mu_s$	sliding friction coefficient
$\rho$	particle density
$\rho_{\text{bulk}}$	poured bulk density
$\rho_{\text{mix}}$	apparent density of polymers in coating liquid
$\rho_{\text{tap}}$	tapped density
$\omega_i$	angular velocity of particle $i$

## References

- Abramoff, M.D., Magelhaes, P.J., Ram, S.J., 2004. Image Processing with ImageJ. *Biophotonics International* 11, 36-42.
- Anand, A., Curtis, J.S., Wassgren, C.R., Hancock, B.C., Ketterhagen, W.R., 2008. Predicting discharge dynamics from a rectangular hopper using the discrete element method (DEM). *Chem. Eng. Sci.* 63, 5821-5830.
- Anand, A., Curtis, J.S., Wassgren, C.R., Hancock, B.C., Ketterhagen, W.R., 2009. Predicting discharge dynamics of wet cohesive particles from a rectangular hopper using the discrete element method (DEM). *Chem. Eng. Sci.* 64, 5268-5275.
- Asmar, B.N., Langston, P.A., Matchett, A.J., Walters, J.K., 2002. Validation tests on a distinct element model of vibrating cohesive particle systems. *Comput. Chem. Eng.* 26, 785-802.
- Beverloo, W.A., Leniger, H.A., van de Velde, J., 1961. The flow of granular solids through orifices. *Chem. Eng. Sci.* 15, 260-269.
- Bierwisch, C., Kraft, T., Riedel, H., Moseler, M., 2009. Three-dimensional discrete element models for the granular statics and dynamics of powders in cavity filling. *J. Mech. Phys. Solids* 57, 10-31.
- Bowden, F.P., Tabor, D., 2001. *The friction and lubrication of solids*. Clarendon Press, Oxford.
- Brown, R.L., Richards, J.C., 1965. Kinematics of the flow of dry powders and bulk solids. *Rheol. Acta* 4, 153-165.
- Carr, R.L., 1965. Evaluating flow properties of solids. *Chem. Eng.-New York* 72, 69-72.

- Castellanos, A., 2005. The relationship between attractive interparticle forces and bulk behaviour in dry and uncharged fine powders. *Adv. Phys.* 54, 263-376.
- Chalykh, A.A., Chalykh, A.E., Novikov, M.B., Feldstein, M.M., 2002. Pressure-sensitive adhesion in the blends of poly(N-vinyl pyrrolidone) and poly(ethylene glycol) of disparate chain lengths. *J. Adhesion* 78, 667-694.
- Cleary, P.W., Sawley, M.L., 2002. DEM modelling of industrial granular flows: 3D case studies and the effect of particle shape on hopper discharge. *Appl. Math. Model.* 26, 89-111.
- Cundall, P.A., Strack, O.D.L., 1979. A discrete numerical model for granular assemblies. *Géotechnique* 29, 47-65.
- Datta, A., Mishra, B.K., Das, S.P., Sahu, A., 2008. A DEM analysis of flow characteristics of noncohesive particles in hopper. *Materials and Manufacturing Processes* 23, 196-203.
- Di Renzo, A., Di Maio, F.P., 2004. Comparison of contact-force models for the simulation of collisions in DEM-based granular flow codes. *Chem. Eng. Sci.* 59, 525-541.
- Eriksson, M., Nyström, C., Alderborn, G., 1993. The use of air permeametry for the assessment of external surface area and sphericity of pelletized granules. *Int. J. Pharm.* 99, 197-207.
- European Pharmacopoeia 7<sup>th</sup> Ed., 2010. Monograph 2.9.36. Powder flow. Strasbourg. Directorate for the Quality of Medicines of the Council of Europe.
- Geldart, D., Abdullah, E.C., Hassanpour, A., Nwoke, L.C., Wouters, I., 2006. Characterization of powder flowability using measurement of angle of repose. *China Part. 4*, 104-107.
- Jerwanska, E., Alderborn, G., Newton, J.M., Nystrom, C., 1995. The effect of water-content on the porosity and liquid saturation of extruded cylinders. *Int. J. Pharm.* 121, 65-71.
- Johansson, B., Wikberg, M., Ek, R., Alderborn, G., 1995. Compression behaviour and compactability of microcrystalline cellulose pellets in relationship to their pore structure and mechanical properties. *Int. J. Pharm.* 117, 57-73.
- Lemieux, M., Bertrand, F., Chaouki, J., Gosselin, P., 2007. Comparative study of the mixing of free-flowing particles in a V-blender and a bin-blender. *Chem. Eng. Sci.* 62, 1783-1802.
- Li, Y.J., Xu, Y., Thornton, C., 2005. A comparison of discrete element simulations and experiments for 'sandpiles' composed of spherical particles. *Powder Technol.* 160, 219-228.
- Luding, S., 2008. Cohesive, frictional powders: contact models for tension. *Granul. Matter* 10, 235-246.
- Nase, S.T., Vargas, W.L., Abatan, A.A., McCarthy, J.J., 2001. Discrete characterization tools for cohesive granular material. *Powder Technol.* 116, 214-223.
- Nedderman, R.M., 1992. *Static and Kinematics of Granular Materials*. Cambridge university press, Cambridge.
- Nedderman, R.M., Tüzün, U., Savage, S.B., Houlsby, G.T., 1982. The flow of granular materials-I: Discharge rates from hoppers. *Chem. Eng. Sci.* 37, 1597-1609.
- Nordstrom, J., Welch, K., Frenning, G., Alderborn, G., 2008. On the physical interpretation of the Kawakita and Adams parameters derived from confined compression of granular solids. *Powder Technol.* 182, 424-435.
- Podczek, F., Newton, J.M., James, M.B., 1995. Adhesion and Friction between Powders and Polymer or Aluminum Surfaces Determined by a Centrifuge Technique. *Powder Technol.* 83, 201-209.
- Salmon, J.K. (1990). *Parallel hierarchial N-body methods*. California Institute of Technology. Pasadena.

- Seville, J.P.K., Willett, C.D., Knight, P.C., 2000. Interparticle forces in fluidisation: a review. *Powder Technol.* 113, 261-268.
- Siiriä, S., Yliruusi, J., 2007. Particle packing simulations based on Newtonian mechanics. *Powder Technol.* 174, 82-92.
- Tao, H., Jin, B., Zhong, W., Wang, X., Ren, B., Zhang, Y., Xiao, R., 2010. Discrete element method modeling of non-spherical granular flow in rectangular hopper. *Chem. Eng. Process.* 49, 151-158.
- Thornton, C., Ning, Z.M., 1998. A theoretical model for the stick/bounce behaviour of adhesive, elastic-plastic spheres. *Powder Technol.* 99, 154-162.
- Train, D., 1958. Some aspects of the property of angle of repose of powders. *J. Pharm. Pharmacol.* 10, T127-T135.
- Tunón, Å., Gråsjö, J., Alderborn, G., 2003. Effect of intragranular porosity on compression behaviour of and drug release from reservoir pellets. *Eur. J. Pharm. Sci.* 19, 333-344.
- Tykhoniuk, R., Tomas, J., Luding, S., Kappl, M., Heim, L., Butt, H.J., 2007. Ultrafine cohesive powders: From interparticle contacts to continuum behaviour. *Chem. Eng. Sci.* 62, 2843-2864.
- Vergheese, T.M., Nedderman, R.M., 1995. The discharge of fine sands from conical hoppers. *Chem. Eng. Sci.* 50, 3143-3153.
- Wikberg, M., Alderborn, G., 1990. Compression characteristics of granulated materials II. Evaluation of granule fragmentation during compression by tablet permeability and porosity measurements. *Int. J. Pharm.* 62, 229-241.
- Wu, C.Y., 2008. DEM simulations of die filling during pharmaceutical tableting. *Particuology* 6, 412-418.
- Zhou, Y.C., Wright, B.D., Yang, R.Y., Xu, B.H., Yu, A.B., 1999. Rolling friction in the dynamic simulation of sandpile formation. *Physica A* 269, 536-553.
- Zhou, Y.C., Xu, B.H., Yu, A.B., Zulli, P., 2001. Numerical investigation of the angle of repose of monosized spheres. *Phys. Rev. E* 64.
- Zhou, Y.C., Xu, B.H., Yu, A.B., Zulli, P., 2002. An experimental and numerical study of the angle of repose of coarse spheres. *Powder Technol.* 125, 45-54.

## Figures

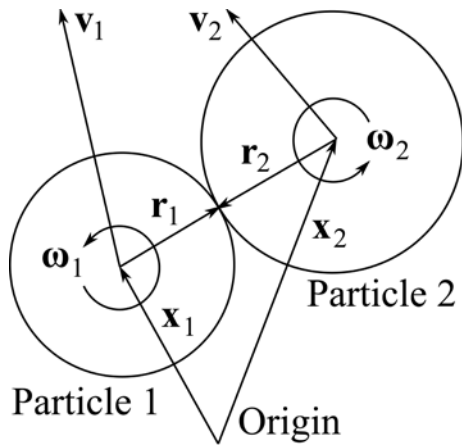


Fig. 1: Contact between two spherical particles.

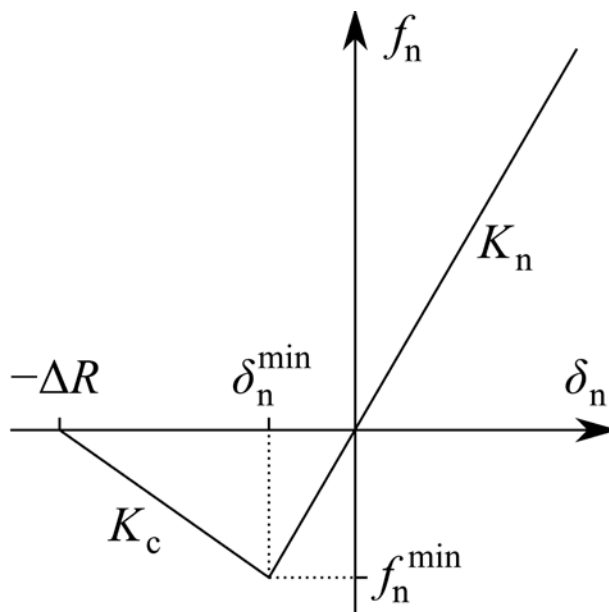


Fig. 2: Normal force  $f_n$  as a function of normal overlap  $\delta_n$ .

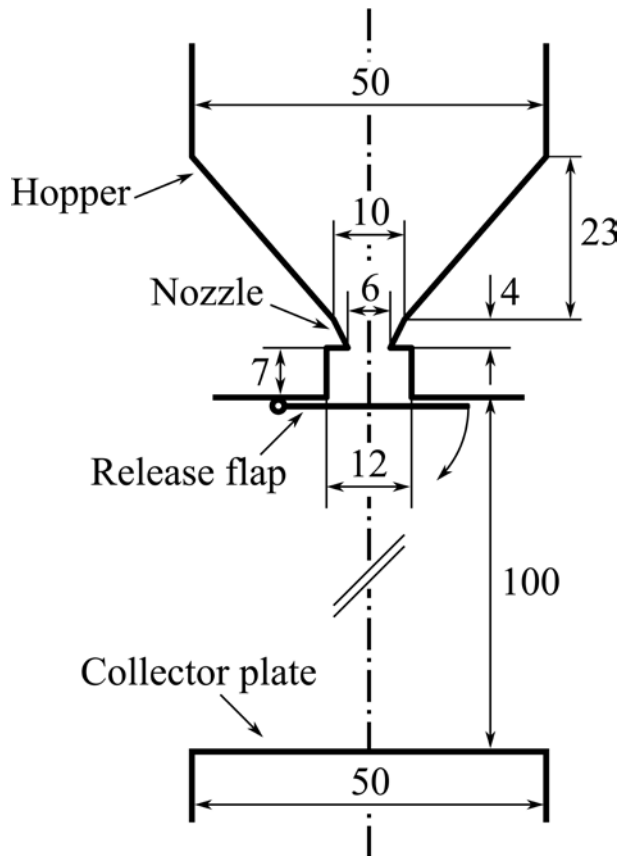


Fig. 3: Geometrical setup used for determinations of angle of repose and discharge rate in experiments and simulations. Numbers indicate distances in mm.

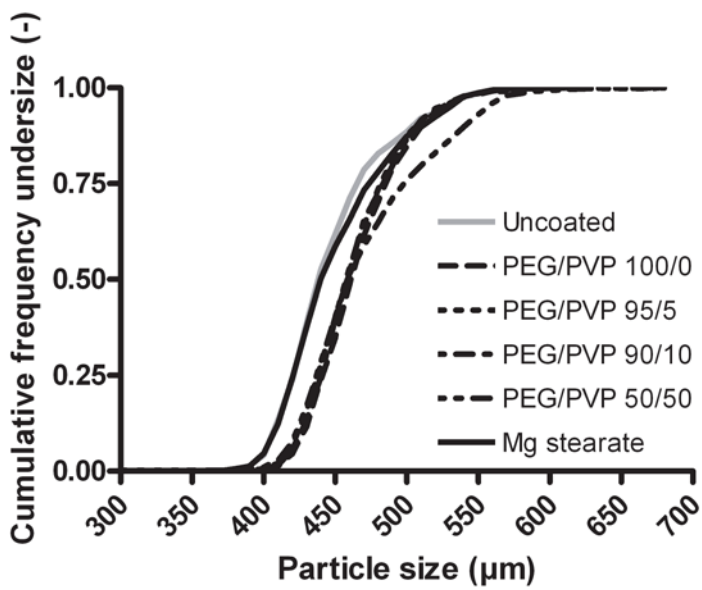


Fig. 4: Particle size distributions for all granule types.

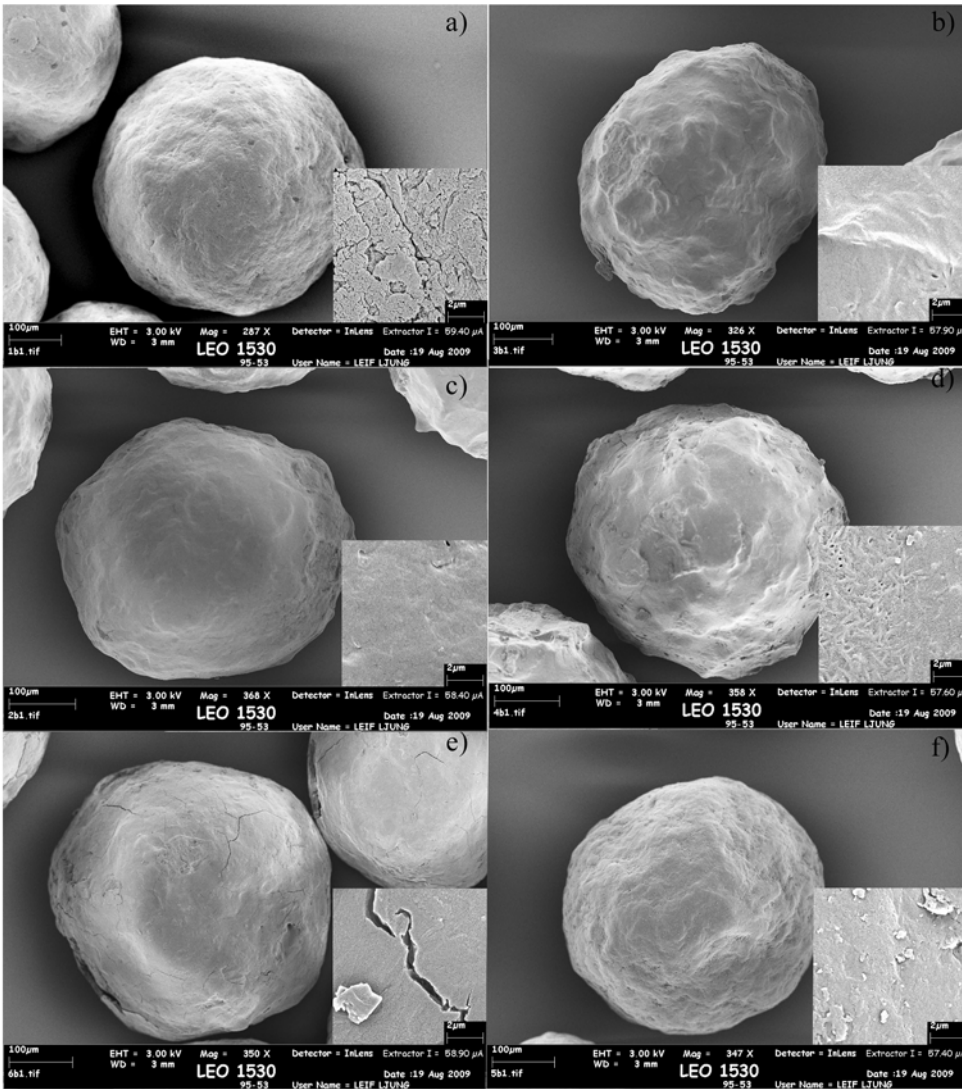


Fig. 5: SEM images of (a) uncoated granules, granules coated with (b) PEG 100, (c) PEG/PVP 95/5, (d) PEG/PVP 90/10, (e) PEG/PVP 50/50 and (f) granules lubricated with magnesium stearate. The insets (10 000 × magnification) display the granule surface morphology.

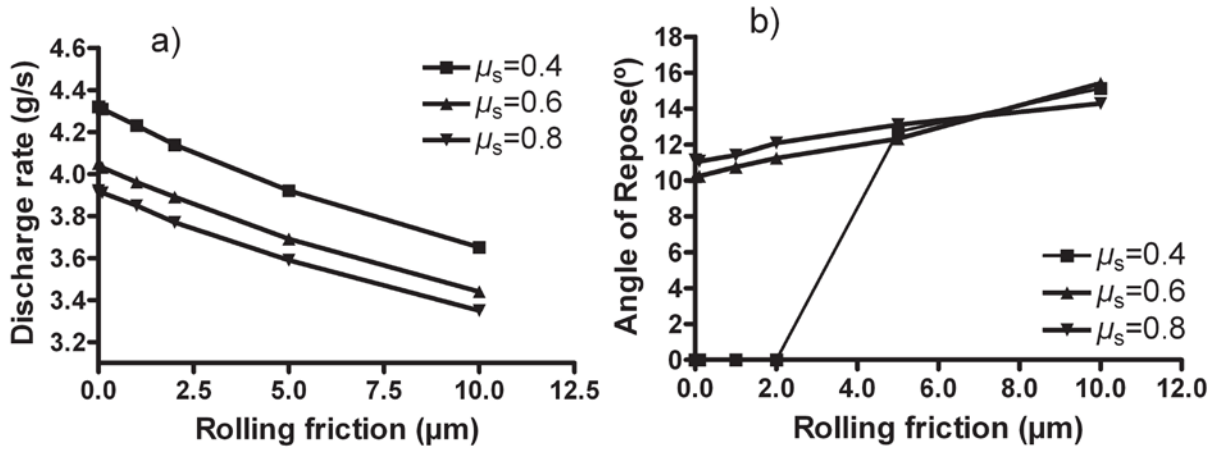


Fig. 6: Relationship between (a) discharge rate and rolling friction ( $\mu_r$ ) and (b) angle of repose and rolling friction, at three sliding friction coefficients ( $\mu_s$ ), for non-cohesive granules.

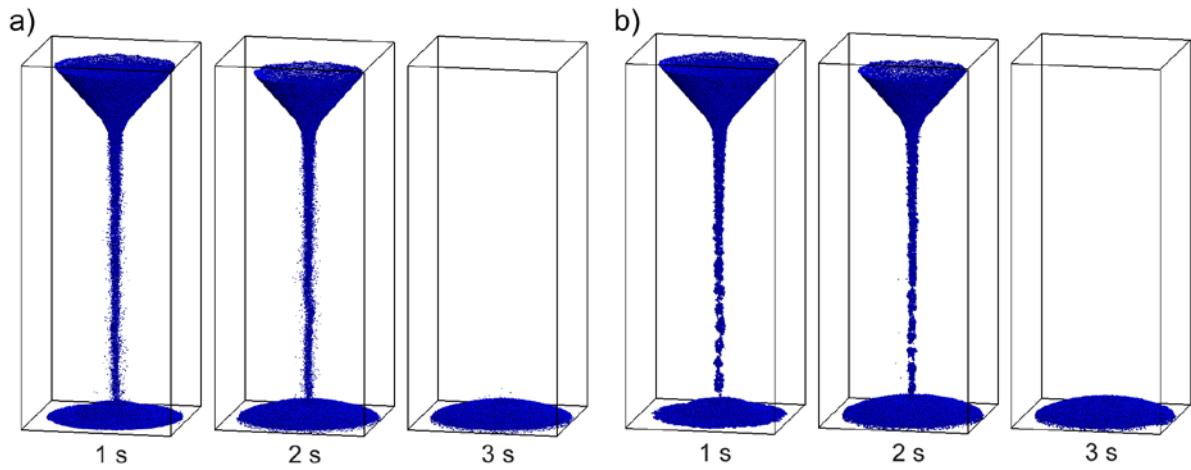


Fig. 7: Illustration of simulated granule flow for (a) non-cohesive particles ( $\mu_s = 0.6$  and  $\mu_r = 2 \mu m$ ) and (b) cohesive particles ( $\mu_s = 0.6$  and  $Bo_g = 2$ ) at three instants of time.

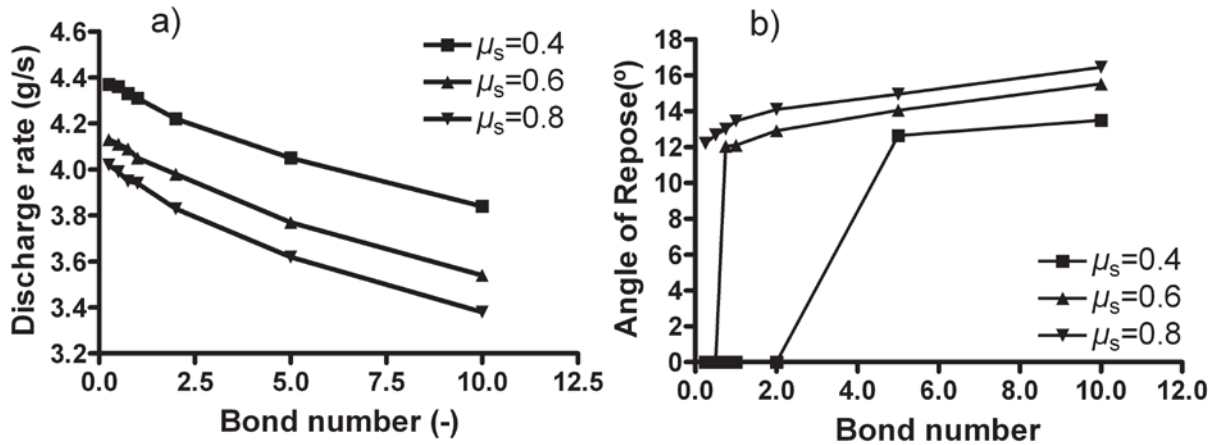


Fig. 8: Relationship between (a) discharge rate and granular Bond number ( $Bo_g$ ) and (b) angle of repose and granular Bond number, at three sliding friction coefficients ( $\mu_s$ ), for cohesive granules.

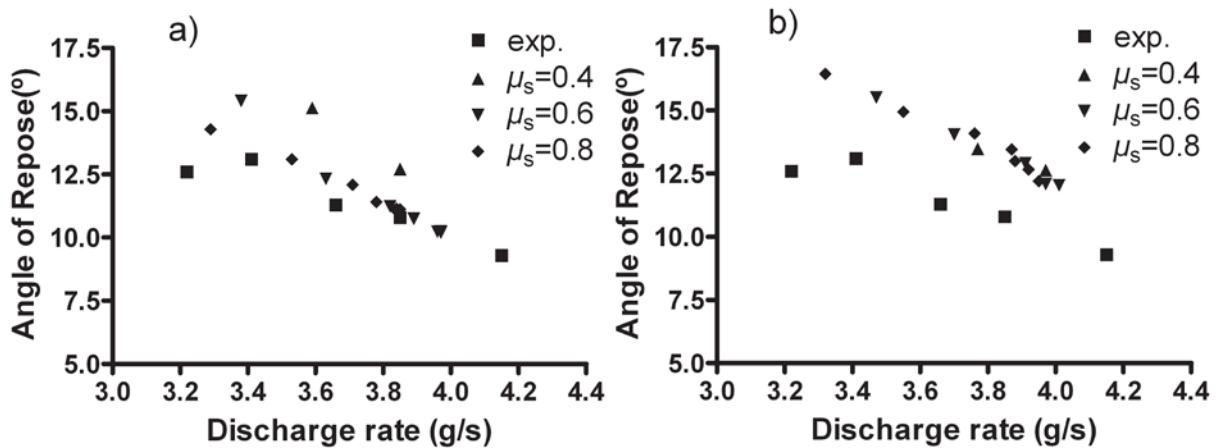


Fig. 9: Comparison of experimental and numerical results displayed as the relationship between angle of repose and discharge rate for (a) non-cohesive granules and (b) cohesive granules. Granules lubricated with magnesium stearate are not included in the figures.

## Tables

Table 1: Granule coating conditions.

Granules	Proportion PEG <sup>a</sup> /PVP <sup>b</sup> (%)	Amount PEG (g)	Amount PVP (g)	Amount magnesium stearate (g)
Uncoated granules	-	-	-	-
PEG/PVP 100/0	100/0	24.38	-	-
PEG/PVP 95/5	95/5	23.12	1.23	-
PEG/PVP 90/10	90/10	21.87	2.43	-
PEG/PVP 50/50	50/50	12.01	12.00	-
Magnesium stearate 1%	-	-	-	0.20

<sup>a</sup>Polyethylene glycol.

<sup>b</sup>Kollidon<sup>®</sup> 17 PF.

Table 2: Fixed parameters in the simulations.

Parameter <sup>a</sup>	Value
$N$	$2 \times 10^5$
$d_p$	425 $\mu\text{m}$
$\rho$	1.414 $\text{g/cm}^3$
$K_n$	125 N/m
$K_t$	125 N/m
$\gamma_n$	0.3
$\gamma_t$	0.3
$\Delta t$	5.0 $\mu\text{s}$

<sup>a</sup>Descriptions of the parameters are found in Sec. 3.5 of the main text.

Table 3: Granule properties. Standard deviations are given in parentheses.

Granules	Median size ( $\mu\text{m}$ )	$\rho_{app}^a$ (g/cm <sup>3</sup> )	$\rho_{eff}^c$ (g/cm <sup>3</sup> )	$\rho_{bulk}^d$ (g/cm <sup>3</sup> )	$\rho_{tap}^e$ (g/cm <sup>3</sup> )	Porosity <sup>f</sup> (%)	Surface area (cm <sup>-1</sup> )	$h^g$ ( $\mu\text{m}$ )
Uncoated granules	442.8	1.57	1.44 (0.01)	0.84 (0.002)	0.91 (0.004)	8.2 (0.55)	189.7 (3.1)	-
PEG/PVP 100/0	465.2	1.52	1.35 (0.05)	0.80 (0.016)	0.84 (0.008)	-	168.5 (0.5)	11.2 (-)
PEG/PVP 95/5	461.1	1.52	1.32 (0.02)	0.83 (0.002)	0.86 (0.002)	-	169.1 (4.2)	9.2 (-)
PEG/PVP 90/10	462.5	1.52	1.39 (0.00)	0.79 (0.007)	0.84 (0.002)	-	168.7 (4.7)	9.9 (-)
PEG/PVP 50/50	463.9	1.52	1.26 (0.05)	0.85 (0.004)	0.88 (0.002)	-	167.9 (2.6)	10.6 (-)
Magnesium stearate	444.2	1.57 <sup>b</sup>	1.42 (0.01)	0.89 (0.007)	0.94 (0.002)	-	184.2 (1.0)	0.7 (-)

<sup>a</sup>Apparent particle densities. For polymer coated granules, the apparent particle densities were calculated as described by Jerwanska et al. (1995)

<sup>b</sup>Assumed to be of the same value as for MCC.

<sup>c</sup>Effective particle densities.

<sup>d</sup>Bulk densities.

<sup>e</sup>Tap densities.

<sup>f</sup>Only calculated for uncoated granules due to assumed unchanged porosity after coating.

<sup>g</sup>Polymer film thickness calculated from the difference in median particle size of the granules.

Table 4: Average sliding friction coefficients ( $n = 10$ ). Standard deviations are given in parenthesis.

Granules	Sliding friction coefficient (-)	
	granule-tablet	granule-paper
Uncoated granules	0.25 (0.03)	0.41 (0.03)
PEG/PVP 100/0	0.30 (0.03)	0.52 (0.07)
PEG/PVP 95/5	0.32 (0.05)	0.48 (0.08)
PEG/PVP 90/10	0.31 (0.03)	0.89 (0.01)
PEG/PVP 50/50	0.30 (0.04)	0.54 (0.11)
Magnesium stearate	0.23 (0.03)	0.42 (0.07)

Table 5: Granule flow properties. Standard deviations are given in parenthesis.

Granules	Angle of repose (°)	Experimental discharge rate (g/s)	$W^a$ (g/s)	$CI^b$ (%)
Uncoated granules	10.8 (0.2)	3.85 (0.08)	3.65 (-)	8.33 (0.58)
PEG/PVP 100/0	12.6 (0.2)	3.22 (0.12)	3.43 (-)	5.00 (1.00)
PEG/PVP 95/5	11.3 (0.1)	3.66 (0.15)	3.54 (-)	4.00 (0.00)
PEG/PVP 90/10	13.1 (0.2)	3.41 (0.13)	3.41 (-)	5.00 (1.00)
PEG/PVP 50/50	9.3 (0.8)	4.15 (0.09)	3.65 (-)	3.67 (0.58)
Magnesium stearate	-	4.01 (0.08)	3.85 (-)	5.67 (0.58)

<sup>a</sup>Beverloo discharge rate calculated using Eq. (14) (Beverloo et al., 1961).

<sup>b</sup>CI=Carr's compressibility index. Calculated as the ratio of the difference between tapped and bulk densities to tapped density.